Journal of Physics: Condensed Matter

PAPER

Critical cation–anion radius ratio and two-dimensional antiferromagnetism in van der Waals $TMPS_3$ (TM = Mn, Fe, Ni)

To cite this article: Valeri Petkov and Yang Ren 2022 *J. Phys.: Condens. Matter* **34** 175404

IOP Publishing Journal of Physics: Condensed Matter
J. Phys.: Condens. Matter **34** (2022) 175404 (11pp) https://doi.org/10.1088/1361-648X/ac527a

Critical cation–anion radius ratio and two-dimensional antiferromagnetism in van der Waals $TMPS_3$ (TM = Mn, Fe, Ni)

Valeri Petkov[1,*] **and Yang Ren**[2,3]

[1] Department of Physics, Central Michigan University, Mt. Pleasant, Michigan 48858, United States of America
[2] X-ray Science Division, Advanced Photon Source, Argonne National Laboratory, Argonne, Illinois 60439, United States of America
[3] Department of Physics, City University of Hong Kong, Kowloon, Hong Kong, People's Republic of China

E-mail: petko1vg@cmich.edu

Received 17 December 2021, revised 4 February 2022
Accepted for publication 7 February 2022
Published 28 February 2022

Abstract

Two-dimensional $TMPS_3$ antiferromagnets, transition metal (TM) = Mn, Fe, Ni, are studied by high-energy x-ray diffraction and atomic pair distribution analysis over a broad temperature range. Results show that the compounds exhibit common average but distinct local atomic structure, including distinct distortions of the constituent TM–S octahedra, magnitude and direction of atomic displacements, TM–TM distances and TM–S–TM bond angles. The differences in the local structure may be rationalized in terms of the Pauling's rule for the critical ratio of TM^{2+} cation and S^{2-} anion radii for octahedral coordination. We argue that the observed differences in the local structure are behind the differences in the antiferromagnetic properties of $TMPS_3$ compounds, including different magnetic anisotropy and Neel temperature.

Keywords: local structure, distortions, total scattering, 2D magnets

Supplementary material for this article is available online

(Some figures may appear in colour only in the online journal)

1. Introduction

Layered transition metal (TM) thiophosphates $TMPS_3$, where TM = Mn, Fe and Ni, have received much interest recently because of their unique magnetic properties, offering promise for practical applications [1–7]. The properties arise from the specific crystal structure, where layers of TM–S_6 octahedra are separated by a van der Waals gap and TM atoms in the layers form a honeycomb lattice, as shown in figure 1. The first, second and even third neighbor TM–TM distances appear shorter than the interlayer separation, thereby weakening the magnetic layer–layer interactions and rendering the compounds 2D magnets [8–10]. In particular, $MnPS_3$, $FePS_3$ and $NiPS_3$ all appear antiferromagnetic at low temperature, where the magnetic moment is due to TM^{2+} ions and the Neel temperature, T_N, is 78, 123 and 155 K, respectively [12–14]. The spin ordering pattern in the different 2D $TMPS_3$ magnets is, however, different. In $MnPS_3$, Mn^{2+} spins are antiferromagnetically coupled with their first neighbors and oriented perpendicularly to the layers. The magnetic susceptibility is largely isotropic and the material appears a good example of a Heisenberg-type antiferromagnet. In $FePS_3$, first neighbor Fe^{2+} spins are ferromagnetically coupled forming parallel zig-zag chains that run in the layers and are antiferromagnetically coupled to each other. The Fe^{2+} spins are oriented perpendicularly to the layers

* Author to whom any correspondence should be addressed.

and the magnetic susceptibly is highly anisotropic, rendering the material a good example of an Ising-type antiferromagnet. Similarly to Fe^{2+} spins in $FePS_3$, Ni^{2+} spins in $NiPS_3$ form ferromagnetic zig-zag chains that run parallel to each other in the layers of Ni–S_6 octahedra and are antiferromagnetically coupled to each other. Contrary to the case of $FePS_3$ and $MnPS_3$, however, Ni^{2+} spins lie in the layers, rendering the material a good example of a Heisenberg antiferromagnet with *xy* anisotropy [15–21]. Given the similarity in the electronic structure of Mn, Fe and Ni species and common crystal structure, the observed differences in the antiferromagnetic properties of TM thiophosphates remains puzzling. Experiments and theory have suggested that the difference may be due to the presence of distinct local structural distortions [8, 13, 21, 24] but this hypothesis has remained largely unexplored. We use a technique that goes beyond traditional crystallography [25–28] to study the local crystal structure of 2D $TMPS_3$ magnets (TM = Fe, Fe, Ni) over a broad temperature range where their magnetic properties change markedly. We find that the compounds do exhibit distinct lattice distortions, including distinct distortions of building TM–S_6 octahedral units, and that the observed differences in their antiferromagnetic properties may be rationalized in terms of the far-reaching concept of structural stability introduced by Pauling and expressed in terms of the ratio of ionic radii of TM and S ions. Our results reveal clearly the presence of a strong relationship between the local structure and properties of 2D magnets and exemplify an efficient experimental approach to study it in fine details.

2. Experiment

High-quality $TMPS_3$ crystals were provided by 2D semiconductors [29]. They were subjected to x-ray-diffraction (XRD) experiments using synchrotron x-rays with energy of 105.7 keV ($\lambda = 0.1173$ Å). Scattered intensities were recorded using a 2D amorphous Si detector in Debye–Scherrer geometry. The detector was positioned 300 mm away from the sample to reach high-q values necessary for atomic pair distribution function (PDF) analysis, where the wave vector q is defined as $q = 4\pi \sin(\theta)/\lambda$ and θ is the Bragg angle. Here it may be added that, due to the azimuthal integration of the Debye–Scherrer rings, the use of a 2D detector helps not only optimize the data collection time and improve the statistical accuracy of the XRD data but also minimize effects of preferred orientation on the data [28, 30, 31], which may occur in diffraction studies on layered materials such as $TMPS_3$. Data in a broad temperature range from 90 to 320 K were collected using Oxford Cryostream 700+ device to control the temperature of the samples. For $NiPS_3$ and $FePS_3$, it includes the para to antiferromagnetic phase transition [11]. For $MnPS_3$ it allows to study the evolution of short-range magnetic correlations observed in the paramagnetic regime down to T_N [13]. Experimental diffraction patterns are summarized in figure 2. Patterns for the different samples are similar, reflecting their common crystal structure type. Positions of corresponding Bragg peaks in the patterns are seen to shift to higher wave vectors with increasing the atomic number, Z, of TM species from Mn(Z = 25) to Fe($Z = 26$) and then to Ni($Z = 28$). The shift reflects the significant difference in the size of Mn^{2+} ($r_{Mn} = 0.83$ Å), Fe^{2+} ($r_{Fe} = 0.78$ Å) and Ni^{2+} ($r_{Ni} = 0.69$ Å) ions for octahedral coordination [32] and leads to a systematic decrease in the lattice parameters of $TMPS_3$ with Z [11, 24]. It has been also been found that the temperature evolution of the lattice parameters becomes nonlinear in the vicinity of T_N [18, 33]. No particular local structure changes relevant to the observed differences in the antiferromagnetic order in $TMPS_3$ compounds, however, has been reported so far.

To obtain more detailed information about the local crystal structure, we considered the experimental XRD patterns in real space in terms of atomic PDFs. The PDFs were derived from the patterns using well-established procedures [34]. The PDFs are shown over an extended range of real-space distances in figures S1, S2, and S3 in supplemental material (https://stacks.iop.org/JPCM/34/175404/mmedia) [35] and appear mapped onto each other in figure 3. The PDFs exhibit well-defined peaks reflecting the presence of well-defined local atomic arrangement in 2D $TMPS_3$ magnets (TM = Mn, Fe, Ni).

Experimental data for the magnetic susceptibility are shown in figure 4. Data were obtained on a Standard Physical Property Measuring system instrument from Quantum Design using the vibrating sample magnetometer mode of operation and are fully consistent with results reported in other studies [11]. As can be seen in the figure, the susceptibility for $MnPS_3$ shows a broad maximum at about 120 K that can be associated with short-range spin–spin correlations [13]. The Neel temperature, defined as the temperature at which the slope of the susceptibility vs temperature curve is maximum, is 78 K. Upon cooling the sample, the susceptibility for $FePS_3$ exhibits a well-defined peak at about 150 K followed by a sharp downturn at $T_N = 123$ K. A characteristic feature of the susceptibility for $NiPS_3$ is the presence of a broad maximum at about 250 K. Below this temperature the material becomes an antiferromagnet at $T_N = 155$ K. The high-temperature behavior of the susceptibility curves for $TMPS_3$ compounds is as expected for paramagnets.

3. Results and discussion

3.1. Average crystal structure

As shown in prior studies [9, 15], $TMPS_3$ compounds adopt a crystal structure with average monoclinic symmetry (S.G. $C12/m1$). To ascertain the crystal structure of studied samples, experimental XRD patterns were subjected to Rietveld analysis. Exemplary Rietveld fits are shown in figure 5. Refined structure parameters are summarized in tables S1–S3 in supplemental material [35]. The fits are of a very good quality indicating that the samples are single phase and no texture effects are present in the XRD data.

3.2. Local crystal structure from analysis of atomic PDFs

The packing of TM and S atomic planes in individual $TMPS_3$ layers, including TM–S and TM–TM bonding distances, type of TM–S coordination polyhedra, including their perfection,

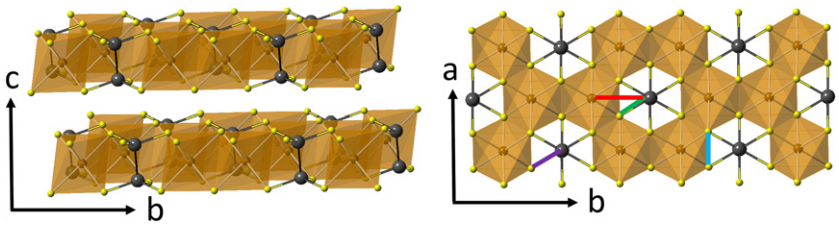

Figure 1. Side (left) and top (right) view of the crystal structure of vdW $TMPS_3$ compounds (TM = Mn, FE, Ni). They can be looked at as layered TMS_2 dichalcogenides, in which one third of TM atoms are replaced by P–P pairs. The replacement takes place in an ordered manner, resulting in the appearing of a honeycomb lattice of edge-sharing TM–S_6 octahedra (brown). Thus P–P pairs appear bonded to six S atoms to form ethane-like $(P_2S_6)^{4-}$ units, where each P atom is tetrahedrally coordinated by three S atoms, and each S atom is bonded to one P atoms and two TM atoms. The layers are held together by weak van der Waals forces. TM, P and S atoms are in brown, black and yellow, respectively. First neighbor P–P, P–S, TM–TM, TM–S and S–S distances are shown as a black, gray, red, green and blue line, respectively. Arrows show the direction of the unit cell vectors of the underlying monoclinic lattice.

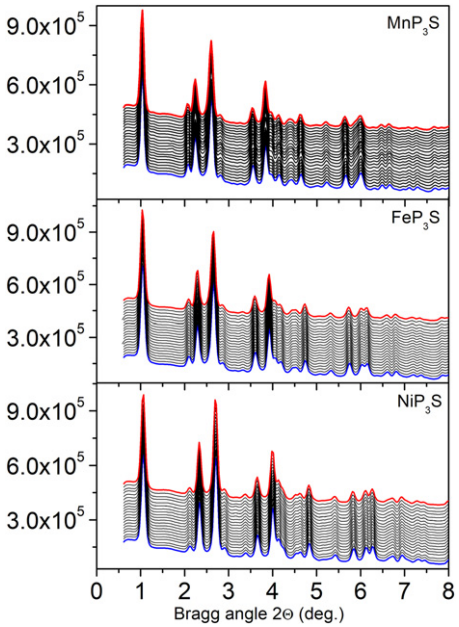

Figure 2. Low-angle part of experimental high-energy XRD patterns for $TMPS_3$ compounds (TM = Mn, Fe, Ni) obtained during their cooling from 320 K (red line) to 90 K (blue line). The patterns show sharp Bragg peaks whose shape and position change little with decreasing temperature.

and character of ethane-like $(P_2S_6)^{4-}$ units, which coordinate each TM ion (see figure 1) and thus participate in spin–spin exchange interactions, have a profound effect on the electronic properties of $TMPS_3$ compounds, including the emergence of antiferromagnetic order. Information for some of these structural parameters can be obtained directly from the experimental PDFs without any assumptions for the compound's crystal structure.

In particular, the shortest interatomic distances in 2D $TMPS_3$ magnets are P–S bonding distances (gray bar in figure 1) in $(P_2S_6)^{4-}$ units. The distances appear as a well-defined but asymmetric first PDF peak, where its major higher-r and weaker low-r components are centered at about 2.05 and 1.98 Å, respectively (see figure 3). Considering that, typically, P–S single and P–S double bonds appear at 2.10 and 1.92 Å, respectively, the P–S bonds in the studied compounds appear to have a strong covalent character. This is not a surprise given the electronegativity, EN, difference between S(EN = 2.58) and P(EN = 2.19) species is rather small. The peak does not change its position and shape with decreasing temperature significantly, reflecting the expected rigidity of P–S bonds. Considering literature data for the ionic radii of S^{2-} and TM^{2+} species [32], the second, well-resolved PDF peak can be ascribed to TM–S bonding distances (green bar in figure 1) in TM–S_6 octahedra. It appears positioned at 2.61, 2.54 and 2.45 Å for TM = Mn, Fe and Ni, respectively, consistent with the well-known differences in their atomic radii. The peak is seen to sharpen significantly with decreasing temperature, indicating diminished positional disorder of TM and S atoms in TM–S_6 octahedra. Here it is to be noted that the experimental TM–S distances appear shorter than the sum of ideal S^{2-} (r_S = 1.84 Å) and TM^{2+} radii, that would be 2.67 Å (vs experimental 2.61 Å), 2.62 Å (vs experimental 2.54 Å) and 2.53 Å (vs experimental 2.45 Å) for Mn, Fe and Ni, respectively. Then, an effective radius of S^{2-} ions in the studied $TMPS_3$ compounds can be computed as a difference of the experimental TM–S bonding distance and well-known ionic radius of the respective TM^{2+} species. The so-computed effective S^{2-} ionic radius in 2D $TMPS_3$ magnets is (2.61 Å − 0.83 Å =) 1.78 Å, (2.54 Å − 0.78 Å =) 1.76 Å and (2.45 Å − 0.69 Å =) 1.76 Å for TM = Mn, Fe and Ni, respectively. The ionicity of TM^{2+}–S^{2-} bond can be computed as a ratio of the effective and ideal S^{2-} radii. It appears to be 0.967, 0.956 and 0.956 for $MnPS_3$, $FePS_3$ and $NiPS_3$, respectively, indicating that the TM–S bonds in 2D $TMPS_3$ magnets are not entirely ionic in character. The higher ionicity of Mn^{2+}–S^{2-} bond in comparison to Fe^{2+}–S^{2-} and Ni^{2+}–S^{2-} bonds reflects the larger difference in the electronegativity of S and Mn species in comparison to Fe(EN = 1.83) and Ni(EN = 1.91) species. The PDF peaks positioned between 3 and 4.5 Å largely reflect first neighbor S–S (blue bar in figure 1) and TM–TM (red bar in figure 1) distances and second neighbor TM–S distances. The peaks are seen to change in both position and shape, indicating that the S and TM sublattices in $TMPS_3$ 2D magnets evolve significantly with decreasing temperature. More information about the evolution was obtained by model fits to the experimental PDFs.

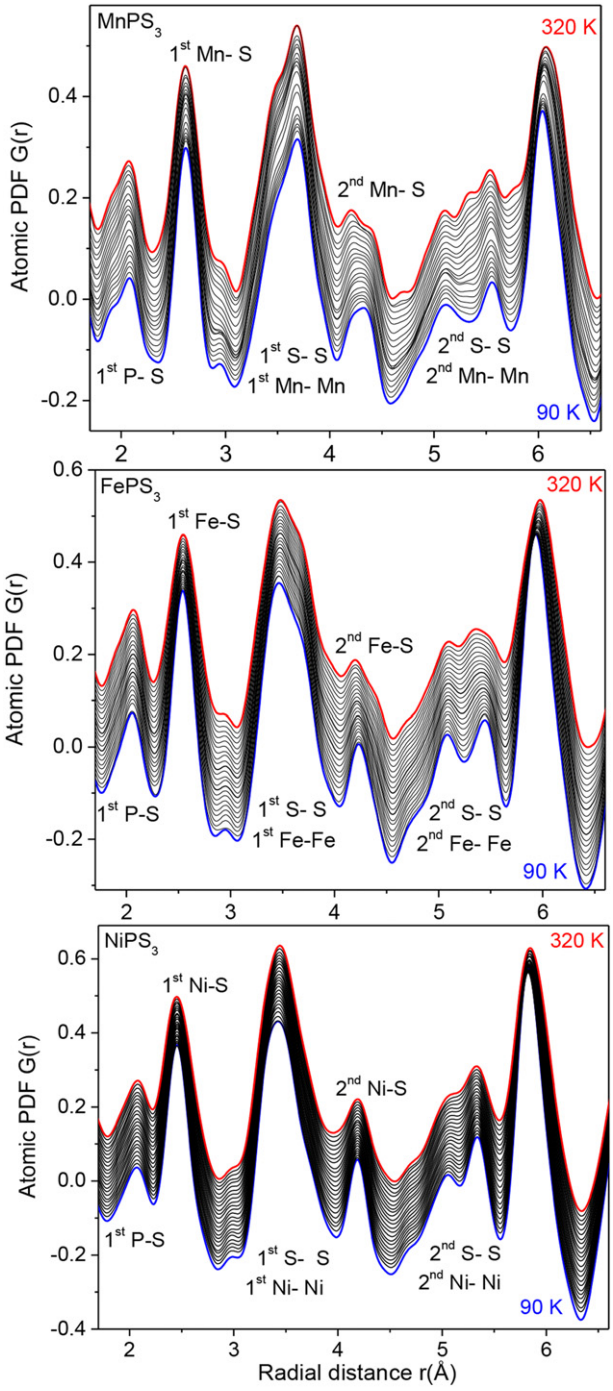

Figure 3. Low-r part of experimental atomic PDFs for $TMPS_3$ compounds (black line), highlighting the evolution of local atomic structure with decreasing temperature from 320 K (red line) to 90 K (blue line). Peaks are labeled with the respective atomic pair distances. Data for TM = Mn, Fe and Ni are shown in the top, middle and lower panel, respectively.

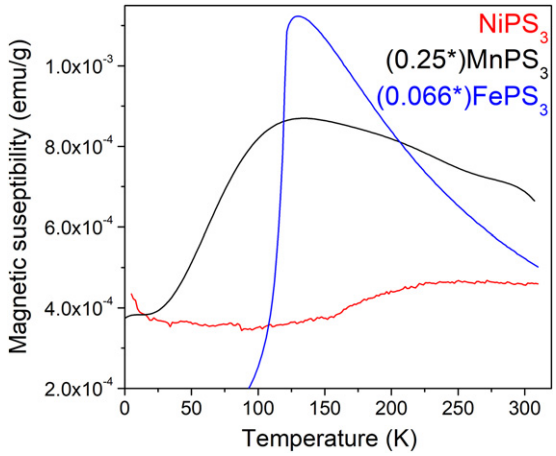

Figure 4. Magnetic susceptibility for $TMPS_3$ compounds (TM = Mn, Fe, Ni) as a function of temperature. The data are fully consistent with results of prior studies [11], indicating the good quality of the samples studied here. As discussed in [11, 17, 24], in general, magnetic data for $TMPS_3$ compounds are consistent with expected magnetic moments for TM^{2+} ions.

3.3. Local crystal structure from modeling of atomic PDFs

Experimental atomic PDFs were fit with a structure model featuring a monoclinic (S.G. $C12/m1$) unit cell suggested by prior structure studies [9, 37] and found successful in explaining the experimental XRD data. Here it may be noted that, as explained in [9], the monoclinicity of $TMPS_3$ compounds is due to the substitution of one third of TM atoms in the nominally hexagonal TMS_2 layers with P–P pairs (see figure 1) and related local lattice distortion. Exemplary results from PDF fits are shown in figure 6. The fits are of a very good quality, confirming that both the local and average crystals structure of 2D $TMPS_3$ magnets is monoclinic. Refined monoclinic lattice parameters and angle are shown in figure 7. Refined thermal factors are shown in figure 8. PDF fits based on a trigonal (S.G. P-31m) crystal structure were also attempted because prior spectroscopy studies have suggested that both thin sheets and bulk $NiPS_3$ may exhibit it [38]. Exemplary results from the fits are shown in figure 9. The fits appeared inferior in comparison to fits based on a monoclinic structure (compare data in figures 6 and 9), confirming that, similarly to bulk $MnPS_3$ and $FePS_3$, bulk $NiPS_3$ is monoclinic.

As can be seen in figure 7, for all $TMPS_3$ studied here, the c lattice parameter, which reflects the vdW gap between $TMPS_3$ layers, diminish uniformly with decreasing temperature. This, however, is not the case with the a and b lattice parameters. For $MnPS_3$, they are seen to evolve non-linearly with decreasing temperature, exhibiting a change in the slope of the temperature evolution at 120 K. The monoclinic angle behaves in a similar way. The observation indicates the presence of significant distortions in the layers. Because magnetic properties of $TMPS_3$ compounds arise largely from intralayer spin–spin interactions, the observed layer distortions may be expected to affect them significantly. Indeed neutron diffraction and Raman studies have identified the presence of significant short-range spin–spin fluctuations and a related single-ion anisotropy antiferromagnetic phase transition in $MnPS_3$ at approximately 120 K [13]. The temperature evolution of the a and b lattice parameters for $FePS_3$ and $NiPS_3$ is also not quite linear. It is seen to change its slope at about 123 and 155 K, respectively, where the para-to-antiferromagnetic transition in these compounds takes place. The same pertains to the respective monoclinic angle.

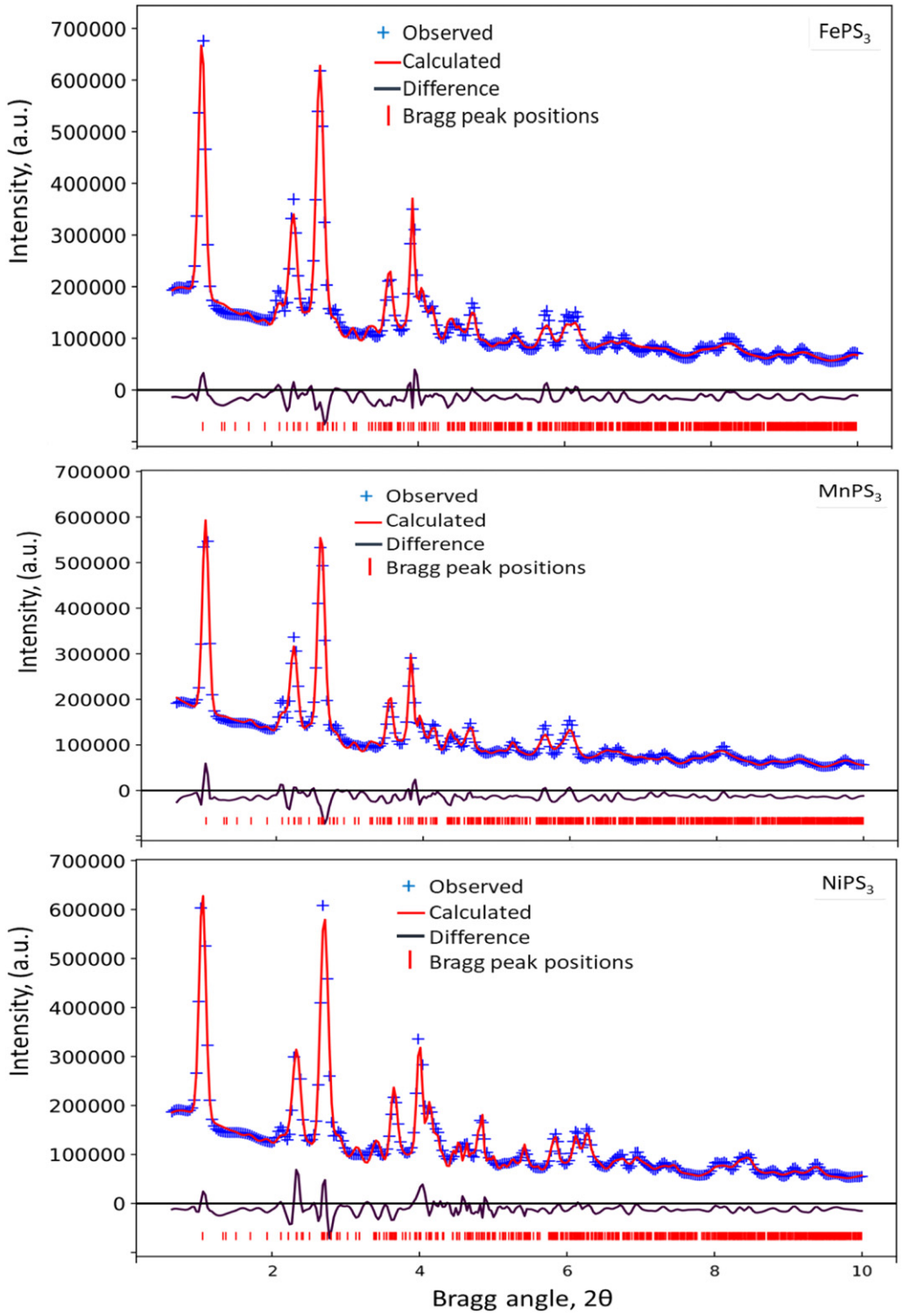

Figure 5. Rietveld fits to XRD patterns for $TMPS_3$ compounds (TM = Mn, Fe, Ni) collected at 90 K. The fits approach the experimental data very well (agreement factor $R_{wp} \sim 6\%$), confirming that the compounds are single phase and possible texture effects on the experimental XRD are insignificant, if any.

As can be seen in figure 8, in-plane and out-of-plane thermal factors for TM, P and S atoms also evolve non-linearly with temperature. As defined, they include trivial, random-type atomic displacements due to thermal excitations and systematic local lattice distortions. The former would gradually disappear with diminishing temperature while the latter would not necessarily exhibit such a trend. Inspection of the data in figure 8 indicates that, in line with results of prior studies [39], the atomic displacements in 2D $TMPS_3$ magnets appear significant and highly anisotropic. In particular, for $MnPS_3$, the out-of-plane displacements of Mn atoms are twice as large as the in-plane displacements. The displacements of P atoms in

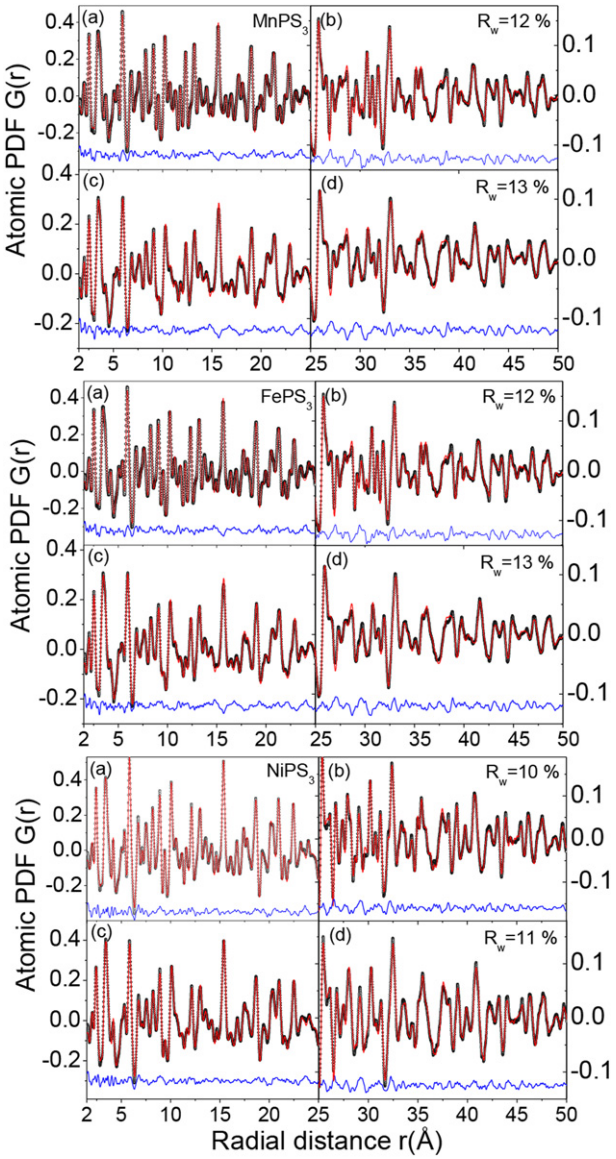

Figure 6. Fits (red line) to experimental (symbols) atomic PDFs for $TMPS_3$ compounds (TM = Mn, Fe, Ni). The fits are based on a monoclinic (S.G. *C*2/*m*) structure model. The low (2–25 Å) and high-*r* (25–50 Å) parts of the data are given on different scales for clarity. The residual difference (blue line) is shifted by subtracting a constant factor. The top, middle and lower panel present data for $MnPS_3$, $FePS_3$ and $NiPS_3$, respectively. Data in (a) and (b) are obtained at 320 K and data in (c) and (d) are obtained at 90 K. The goodness-of-fit indicator, R_w, is given for each fit. Here is to be noted that the goodness-of-fit factors resulting from PDF fits appear larger (10%–15%) than those achieved in Rietveld fits to XRD patterns (5%–10%). This is because PDFs fits account for both the diffuse and Bragg-like components of the diffraction patterns while Rietveld fits are sensitive to the latter alone. Note that the PDF data range from 2 to 50 Å includes four unit cells of $TMPS_3$ compounds, i.e., largely, it is sensitive to their local atomic structure.

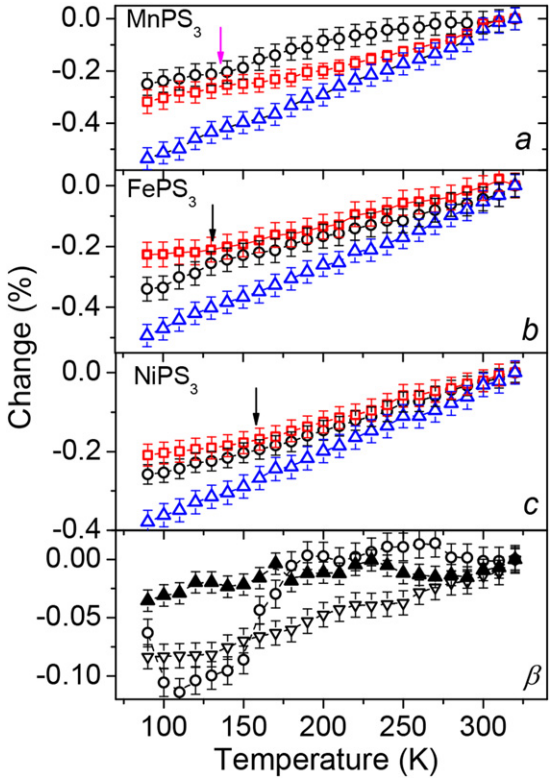

Figure 7. Change in the monoclinic lattice parameters *a* (red), *b* (black) and *c* (blue) for $TMPS_3$ compounds as a function of temperature (TM = Mn, Fe, Nj). Change in the monoclinic angle β is also shown (empty triangles for Fe, full triangles for Ni and circles for Mn). Data are obtained by fits to atomic PDFs. Black arrows indicate the magnetic phase transition temperature, T_N, for $FePS_3$ and $NiPS_3$ determined from magnetic susceptibility data (see figure 4). Magenta arrow indicates the onset of short-range order magnetic fluctuations and single-ion anisotropy related phase transition in $MnPS_3$ observed by neutron diffraction and Raman spectroscopy [13]. Broken lines are a guide to the eye. Error bars are given for each data set.

$MnPS_3$ show a similar trend. For S(1) atoms, which are sandwiched between the chains of Mn atoms as shown in figure 10, the situation is reversed. In-plane and out-of-plane displacements of S(2) are comparable in magnitude at room temperature alone. Below 150 K, however, the latter increase steeply, indicating increased atomic positional disorder, whereas the former keep diminishing gradually. The in-plane displacements for Mn, P and S(1) show a similar upturn when temperature approaches 120 K upon cooling, confirming that, largely, the temperature driven structure changes in $MnPS_3$ take place in the *ab* planes.

The in-plane displacements for Fe atoms in $FePS_3$ are much smaller than those for Mn atoms in $MnPS_3$ whereas the out-of-plane ones are comparable. The displacements of P atoms in $MnPS_3$ and $FePS_3$ also appear comparable. The displacements of S(1) and S(2) atoms in the latter, however, appear smaller in comparison to the former.

Contrary to the case of $MnPS_3$ and $FePS_3$, in $NiPS_3$, both in and out-of-plane displacements of TM(Ni), P, and S(1) species from their average positions in the crystal lattice appear similar in magnitude. The exception is S(2) species, which are seen to undergo markedly large out-of-plane displacements from room temperature down to 90 K. Overall, not only $TMPS_3$ compounds exhibit systematic and highly anisotropic lattice distortions with diminishing temperature, as measured by the large anisotropy of atomic displacements, but also the

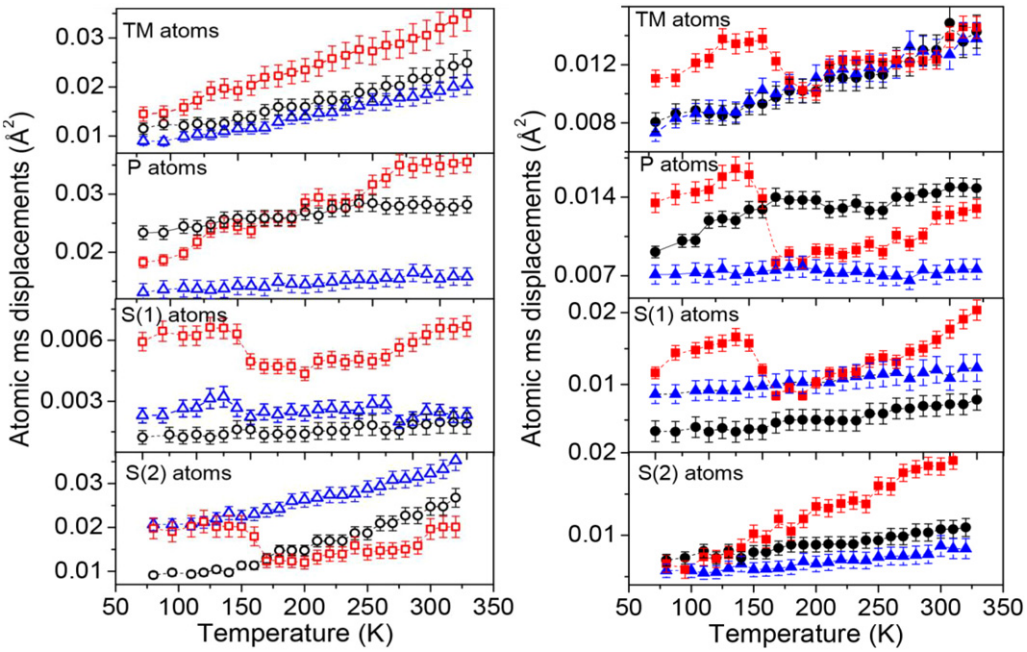

Figure 8. Change in the out-of-plane (left; open symbols) and in-plane (right, closed symbols) displacements of TM, P, S(1) and S(2) atoms in $TMPS_3$ compounds as a function of temperature, where TM = Mn (red), Fe(black) and Ni (blue) Data are obtained by fits to atomic PDFs. Broken lines are a guide to the eye. The inequivalent S(1) and S(2) atoms in the crystal structure of $TMPS_3$ compounds are shown in figure 10. Error bars are given for each data set.

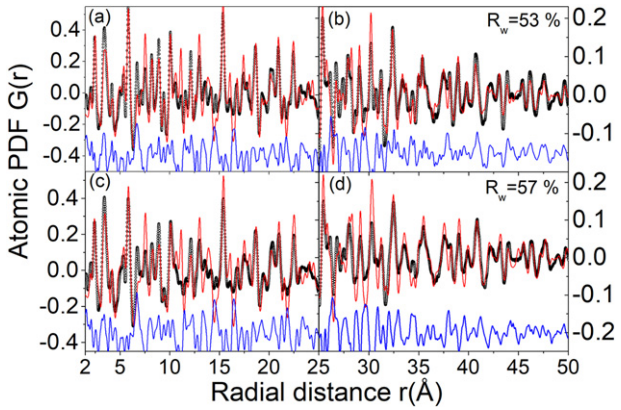

Figure 9. Fits (red line) to experimental (symbols) atomic PDFs for $NiPS_3$ obtained at 320 K (upper panel) and 90 K (lower panel). The fits are based on a trigonal (S.G. *P*-31*m*) structure model. The low (a), (c) and high-*r* (b), (d) parts of the data are given on different scales for clarity. The residual difference (blue line) is shifted by subtracting a constant factor. The goodness-of-fit indicator, R_w, is given for each fit.

magnitude of these distortions depends on the type of TM species.

3.4. Origin of anisotropic lattice distortions in $TMPS_3$ compounds

To understand the reason behind the observed anisotropy of local lattice distortions, we considered the $TMPS_3$ crystal structure in terms of closed packed layers of large spherical S anions with small TM cations occupying interstices between the anions. In such a consideration, introduced by Pauling [40, 41], the cations would appear surrounded by anions forming polyhedra, where the ratio of cation to anion radii, r^+/r^-, determines the shape and stability of the latter. In particular, the so-called ideal radius ratio for which the cation (TM^{2+}) would be in an optimal contact with the nearby anions (S^{2-}) and, hence, the resulting TM–S_6 octahedra in $TMPS_3$ compounds would be stable and undistorted, is 0.414 [40]. When the ratio is greater than 0.414, the six S^{2-} ions would be pushed further from each other so that their mutual repulsion is reduced, resulting in a distortion of the TM–S_6 octahedra. When the radius ratio is less than 0.414, two S^{2-} ions would tend to depart and the remaining four to rearrange to optimize TM^{2+}–S^{2-} bonds. This would also result in a local lattice distortion, whose type, however, would be different from that observed when $r^+/r^- > 0.414$ [36, 40, 41]. The critical r^+/r^- radius ratio for 2D $TMPS_3$ magnets, computed from the TM^{2+} and effective S^{-2} radii listed above, are shown in figure 11. Also shown in the figure are the ratio of the refined *b* and *a* parameters of the monoclinic lattice, indicative of the distortions in the $TMPS_3$ layers, including TM–S_6 octahedra, and monoclinic angle β, indicative of the distortions in the $TMPS_3$ layer packing sequence. Note that the ideal *b*/*a* ratio is $\sqrt{3} = 1.732$ and the ideal β is 107.16° [9]. As can be seen in the figure, the coordination polyhedra and layer packing in $TMPS_3$ 2D magnets are not quite perfect and the deviation from perfectness is different for the different compounds. That is, following Pauling's rules, octahedra in $MnPS_3$ and $FePS_3$ appear expanded while those in $NiPS_3$ appear flattened, leading to a distribution of TM–S bonding distances in the respective compounds. In particular, from the refined structure models, it can be computed that first neighbor Mn–S distances in $MnPS_3$ appear as two long (2.65 Å) and four short (2.62 Å) bonds.

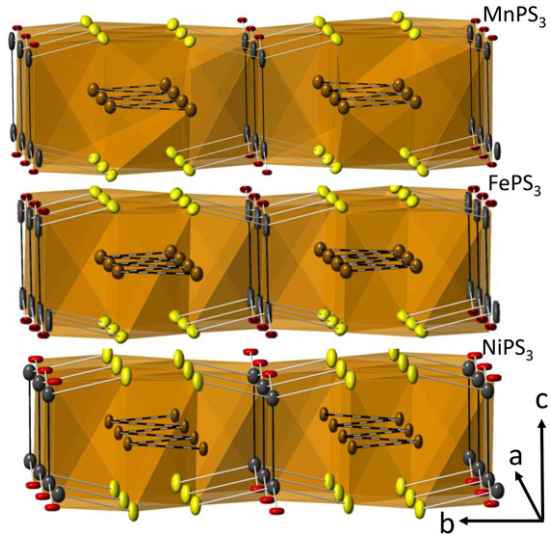

Figure 10. Fragment from $TMPS_3$ compounds, where zig-zag chains of TM atoms (TM = Mn, Fe, Ni) run in parallel to the *a* axis of the monoclinic lattice and P atoms (black) are coordinated by two types of sulfur atoms, referred to in the text as S(1) and S(2) atoms. In particular, S(1) atoms, given in red, appear sandwiched between the zig-zag chains and S(2) atoms, given in yellow, are positioned above and below the chains. The preferred direction of atomic displacements experienced by the two inequivalent S atoms is different in each compound. The amplitude of the displacements of TM and P atoms in the different compounds is also different. All atoms are represented by their 'thermal ellipsoids' derived by fits to atomic PDFs obtained at 90 K, where thermal excitations are significantly quenched in comparison to room *T*. Therefore, the ellipsoids are representative of positional disorder of the respective atoms. The ellipsoids are rather anisotropic, reflecting the local anisotropy in the distortion of constituent octahedra in $TMPS_3$ compounds, as measured by the deviation of the respective r^+/r^- value from the ideal for octahedral coordination.

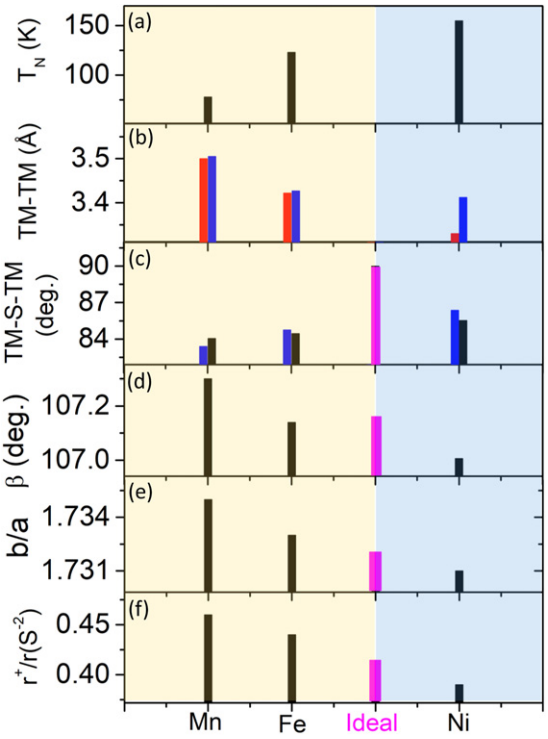

Figure 11. (a) Antiferromagnetic Neel temperature T_N for $TMPS_3$ compounds, where TM = Mn, Fe and Ni. (b) Distances between TM atoms forming chains (red bars) and TM atoms from different chains (blue bars) shown in figure 12. (c) TM–S–TM angles Φ' (black bars) and Φ'' (blue bars) shown in figure 12. (d) Monoclinic angle β computed as $\cos^{-1}(-a/3c)$, where *a* and *c* are the parameters of monoclinic lattice for $TMPS_3$, (e) ratio of the *b* and *a* parameters of the monoclinic lattice. (f) Cation to anion radius ratio, r^+/r^-, in $TMPS_3$ compounds obtained as described in the text. Here the magenta bar indicates the ideal for octahedral coordination r^+/r^- value of 0.419. The magenta bar in (e) indicates the ideal value for *b*/*a* of $\sqrt{3}$ (=1.732) explained in reference [9]. The magenta bar in (f) indicates the ideal monoclinic angle of 107.16° also explained in reference [9]. Area shaded in light brown color highlights data for $MnPS_3$ and $FePS_3$, where r^+/r^-, *b*/*a* and β are larger than the ideal values, octahedra are expanded, atomic displacements of TM atoms centering the octahedra are significant (see figures 7, 8 and 10) and spins are perpendicular to the (*ab*) plane of the monoclinic lattice. Area shaded in light blue color highlights data for $NiPS_3$, where r^+/r^-, *b*/*a* and β are smaller than the ideal values, octahedra are flattened and twisted, atomic displacements of Ni atoms centering the octahedra are reduced in comparison to both $MnPS_3$ and $FePS_3$ (see figures 7 and 9) and spins lie in the (*ab*) plane of the monoclinic lattice. Structure data in (b)–(f) are derived from fits to PDF data obtained at 90 K.

In $FePS_3$, Fe–S bonds are also grouped into two long (2.55 Å) and four short (2.53 Å) bonds, where the difference between the former and latter is smaller in comparison to $MnPS_3$. By contrast, Ni–S bonds in $NiPS_2$ appear grouped into two long (2.50 Å), two medium (2.46 Å) and two short bonds (2.42 Å). Implications on the magnetic properties are discussed below.

3.5. Local structure—antiferromagnetic properties relationship for $TMPS_3$ compounds

The type of magnetic order in $TMPS_3$ compounds is determined by the filling of the *d* orbitals of TM ions, magnitude and sign of interactions between the spins of first, second and third TM–TM neighbors, labeled as J_1, J_2 and J_3 in figure 12, and magnetic anisotropy. The interactions could have a direct and indirect component and the anisotropy is strongly influenced by the monoclinic distortion of the crystal lattice [11, 17]. Direct interactions would contribute to the sign and magnitude of J_1 alone and are known to depend on first neighbor TM–TM distances. Theoretical studies [41] have indicated that the direct exchange would be antiferromagnetic for $MnPS_3$, ferromagnetic for $FePS_3$ and nonexistent for $NiPS_3$ because the relevant to magnetism t_{2g} orbitals are filled for Ni^{2+} ions. Indirect interactions are superexchange in character and mediated by S atoms on the vertices of edge-sharing octahedra centered by TM atoms. They would contribute to all J_1, J_2 and J_3. As found by experiment [11, 14, 16] and predicted by Goodenough–Kanamori rules [42–44], $MnPS_3$ has a nearest-neighbor exchange that is negative ($J_1 < 0$). That exchange interaction is positive ($J_1 > 0$), i.e. ferromagnetic, for $FePS_3$ and $NiPS_3$. Notably, the strength of this interaction is known to depend on the TM–S–TM bond angles. Data for the first neighbor TM–TM distances, TM–S–TM

bond angles and Neel temperature T_N for $TMPS_3$ 2D magnets are shown in figure 11. As can be seen in the figure, the relatively large in size Mn atoms induce significant local lattice distortions, as measured by the relatively large deviation of r^+/r^-, b/a and β from the ideal values. In addition, Mn–S–Mn bond angles appear smaller and Mn–Mn distances appear longer than TM–S–TM bond angles and TM–TM distances in $FePS_3$ and $NiPS_3$, respectively, eventually leading to diminished exchange interactions and T_N (78 K). On the other hand, Ni–S–Ni bond angles appear closer to 90° and Ni–Ni distances appear shorter in comparison to TM–S–TM angles and TM–TM distances in $FePS_3$ and $MnPS_3$, respectively, eventually leading to increased exchange interactions and T_N (155 K). First neighbor Fe–Fe distances, Fe–S–Fe bond angles and T_N (123 K) in $FePS_3$ appear in between TM–S–TM angles, TM–TM separation and T_N for $MnPS_3$ and $NiPS_3$. Furthermore, as shown by theoretical investigations relevant to van der Waals TM dichalcogenides [45, 46], different in type deformations of TM–S octahedra may render the magnetic anisotropy in the respective compounds different. This may explain why the spin patterns in antiferromagnetic $NiPS_3$, where the octahedra are flattened, and that in antiferromagnetic $FePS_3$ and $MnPS_3$, where the octahedra are expanded, are different. In particular, spins in the former lie in the *ab* plane whereas those in the latter are orthogonal to it. When TM–S_6 octahedra are very significantly distorted, i.e. when the r^+/r ratio is very different from the ideal value, though present, the magnetic anisotropy may appear less well defined. Accordingly, the spin pattern may also appear strongly influenced by dipole–dipole interactions, which is the case of Heisenberg antiferromagnet $MnPS_3$ [22]. Further theoretical studies accounting for the different distortions of TM–S_6 octahedra in different 2D $TMPS_3$ 2D magnets are necessary to clarify this point.

Rendition of the honeycomb lattice of TM species with the exchange interaction between their spins, including TM–S–TM bond angles relevant to the magnitude and sign of the interactions, is shown in figure 12. Results from PDF fits show that, for all 2D $TMPS_3$ antiferromagnets studied here, the first neighbor TM–TM distances (red arrows in figure 12) and TM–S–TM bond angles (Φ' in figure 12) along the zig-zag chains of TM atoms are different from those involving TM atoms from different chains (blue arrows and Φ'' in figure 12). Such differences could affect the magnetic properties noticeably, as predicted by DFT and found in the case of $FePS_3$ [23, 24].

Local structure features can also explain recently observed unusual electronic properties of $TMPS_3$ compounds. In particular, analysis of the PDF refined structure models reveals a peculiar evolution of P–P bond, whose length is commensurate with the thickness of $TMPS_3$ layers, with temperature. For $MnPS_3$, it diminishes from 2.394 Å at 320 K to 2.295 Å at 90 K. For $FePS_3$, it diminishes from 2.228 Å at 320 K to 2.212 Å at 90 K. For $NiPS_3$, likely due to the inherent flattening of constituent octahedra and built from them layers, it does not change much with temperature, remaining close to 2.126 Å over the temperature region studied here. Not surprisingly, contrary to the case of $MnPS_3$ and $FePS_3$, a P–P stretch mode does not appear in the near-field infrared spectra for $NiPS_3$ [38]. Lastly, analysis of PDF refined structure models indicates that short P–S bonds (1.98 Å) involve S(1) atoms (red in figure 10) sandwiched between zig-zag chains of TM atoms while long P–S bond (2.08 Å) involve S(2) atoms positioned along the chains (yellow in figure 10). The different charge density distribution in the inequivalent P–S(1) short and P–S(2) long bonds would lead to the emergence of stripes with different charge density running in parallel to the chains of TM atoms. As discussed in reference [47], the emerging of such stripes goes hand in hand with the appearing of spin–orbit-entangled excitons in $NiPS_3$.

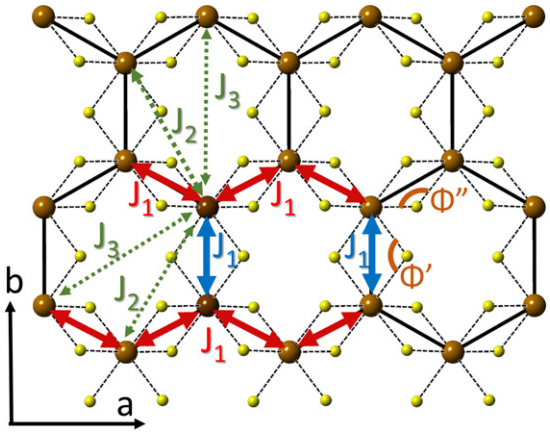

Figure 12. TM and S atom sublattices in $TMPS_3$ compounds projected onto the (*ab*) plane of the monoclinic lattice. First, second and third TM–TM neighbor exchange interactions are given as J_1, J_2 and J_3, respectively. First TM–TM exchange interactions between atoms forming zig-zag chains that run along the *a* axis of the monoclinic lattice are highlighted in red. First TM–TM exchange interactions between atoms from nearby parallel chains are highlighted in blue. TM–S–TM bond angles associated with the former and latter are marked as Φ' and Φ'', respectively. Solid black lines highlight the honeycomb lattice of TM atoms and broken lines denote first neighbor TM–S distances. TM and S atoms are given as brown and yellow circles, respectively. Note that S atoms are positioned above and below the plane of TM atoms and though Φ' and Φ'' appear larger than 90° their values are actually close to 85°.

4. Conclusion

On average, 2D $TMPS_3$ magnets exhibit a common monoclinic crystal structure. Locally, however, they exhibit distinct lattice distortions that affect their antiferromagnetic properties significantly. The distortions may be rationalized in terms of the Pauling's rule for the critical ratio of the radii of TM^{2+} and S^{2-} ions. In particular, due to the small size of TM(Ni^{2+}) cation in $NiPS_3$, TM–S bonds are relatively short, TM–S–TM angles approach 90° and r^+/r^- ratio is smaller than the critical for octahedral coordination. Accordingly, flattened TM–S_6 octahedra accommodate TM spins lying in the *ab* plane, rendering the material a *xy*-type antiferromagnet, and T_N is as high as 155 K. Due to the increased size of TM(Fe^{2+}) cation in $FePS_3$, the length of TM–S bonds and deviation of TM–S–TM

angle from 90° appear increased in comparison to $NiPS_3$. Furthermore, the r^+/r ratio is larger than the critical for octahedral coordination. Accordingly, TM spins in expanded TM–S_6 octahedra are orthogonal to the *ab* plane, rendering the material an Ising-type antiferromagnet, and T_N appears diminished to 123 K. Due to the further increased size of TM(Mn^{2+}) cation in $MnPS_3$, TM–S bonds, deviation of TM–S–TM angle from 90° and r^+/r^- ratio are further increased in comparison to $FePS_3$. Accordingly, Mn spins in further expanded Mn–S_6 octahedra are less restrained to rotate about the *ab* plane in comparison to Fe spins in $FePS_3$, rendering the material a Heisenberg-type antiferromagnet, and T_N appears further diminished to 78 K. Given the strong correlation between the antiferromagnetic properties and local structural distortions in van der Waals $TMPS_3$ compounds, efforts to tune the properties of 2D magnets by rational design guided by simple but fundamental principles obeyed by physical systems such as Pauling's rules appear worthwhile.

Acknowledgments

This work was supported by the U.S. Department of Energy, Office of Science, Office of Basic Energy Sciences under Award No. DE-SC0021973 and used resources of the Advanced Photon Source at the Argonne National Laboratory provided by the DOE Office of Science under Contract No. DE-AC02-06CH11357.

Supplementary materials

Experimental atomic pair distribution functions and results from Rietveld and PDF fits.

Data availability statement

The data that support the findings of this study are available upon reasonable request from the authors.

ORCID iDs

Valeri Petkov https://orcid.org/0000-0002-6392-7589

References

[1] Han D, Ogura M, Held A and Ebert H 2020 Unique behavior of halide double perovskite with mixed halogens *ACS Appl. Mater. Interfaces* **12** 37100–7

[2] Mayarga-Martinez C C, Sofer Z, Sedmidubsky D, Huber S, Eng A Y and Pumera M 2017 Layered metal thiophosphate materials: magnetic, electrochemical and electronic properties *ACS Appl. Mater. Interfaces* **9** 12563–73

[3] Tang W, Liu H, Li Z, Pan A and Zeng Y-J 2021 Spin–orbit torque in van der Waals-layered materials and heterostructures *Adv. Sci.* **8** 2100847

[4] Ray S and Das T 2021 Hierarchy of multi-order skyrmion phases in twisted magnetic bilayers *Phys. Rev.* B **104** 014410

[5] Samal R, Sanyal G, Chakraborty B and Rout C S 2021 Two-dimensional transition metal phosphorous trichalcogenides (MPX_3): a review on emerging trends, current state and future perspectives *J. Mater. Chem.* A **9** 2560–91

[6] Xu D *et al* 2020 Controllable nonlinear optical properties of different-sized iron phosphorus trichalcogenide ($FePS_3$) nanosheets *Nanophotonics* **9** 4555

[7] Khan Y, Obaidulla S M, Habib M R, Gayen A, Liang T, Wang X and Xu M 2020 Recent breakthroughs in two-dimensional van der Waals magnetic materials and emerging applications *Nano Today* **34** 100902

[8] Wang P, Abudoureheman M and Chen Z 2020 Experimental and theoretical studies of the ternary thiophosphate $PbPS_3$ featuring ethane-like $[P_2S_6]^{4-}$ units *Dalton Trans.* **49** 17221–9

[9] Ouvrard G and Brec R 1990 Chalcogen stacking and symmetry: application to layered chalcogenophosphates MPX_3 *Eu. J. Solid State Ing. Chem* **27** 477–88

[10] Wang F *et al* 2018 New Frontiers on van der Waals layered metal phosphorous trichalcogenides *Adv. Funct. Mater.* **28** 1802151

[11] Joy P A and Vasudevan S 1992 Magnetism in the layered transition-metal thiophosphates MPS_3 (M = Mn, Fe, and Ni) *Phys. Rev.* B **46** 5425–33

[12] Lançon D, Ewings R A, Guidi T, Formisano F and Wildes A R 2018 Magnetic exchange parameters and anisotropy of the quasi-two-dimensional antiferromagnet $NiPS_3$ *Phys. Rev.* B **98** 134414

[13] Wildes A R, Kennedy S J and Hicks T J 1994 True two-dimensional magnetic ordering in $MnPS_3$ *J. Phys.: Condens. Matter.* **6** L355–41
Sun Y-J, Tan Q-H, Liu X-L, Gao Y-F and Zhang J 2019 Probing the magnetic ordering of antiferromagnetic $MnPS_3$ by Raman spectroscopy *J. Phys. Chem. Lett.* **10** 3087–93

[14] Goossens D J, Wildes A R, Ritter C and Hicks T J 2000 Ordering and the nature of the spin flop phase transition in $MnPS_3$ *J. Phys.: Condens. Matter.* **12** 1845–54

[15] Wildes A R *et al* 2015 Magnetic structure of the quasi-two-dimensional antiferromagnet $NiPS_3$ *Phys. Rev.* B **92** 224408

[16] ur Rehman Z, Muhammad Z, Moses O A, Zhu W, Wu C, He Q, Habib M and Song L 2018 Magnetic isotropy/anisotropy in layered metal phosphorous trichalcogenides MPS_3 (M = Mn, Fe) single crystals *Micromachines* **9** 29

[17] Koo H-J, Kremer R and Whangbo M-H 2021 Unusual spin exchanges mediated by the molecular anion $P_2S_6^{4-}$: theoretical analyses of the magnetic ground states, magnetic anisotropy and spin exchanges of MPS_3 (M = Mn, Fe, Co, Ni) *Molecules* **26** 1410

[18] Jernberg P, Bjarman S and Wäppling R 1984 $FePS_3$: a first-order phase transition in a '2D' Ising antiferromagnet *J. Magn. Magn. Mater.* **46** 178–90

[19] Basnet R, Wegner A, Pandey K, Storment S and Hu J 2021 Highly sensitive spin-flop transition in antiferromagnetic van der Waals material MPS_3 (M = Ni and Mn) *Phys. Rev. Mater.* **5** 064413

[20] Chanfrasekharan N and Vasudevan S 1994 Magnetism, exchange and crystal field parameters in the orbitally quenched Ising antiferromagnet $FePS_3$ *Pramana* **43** 21–31

[21] Rule K C, Kennedy S J, Goossens D J, Mulders A M and Hicks T J 2002 Contrast antiferromagnetic order between $FePS_3$ and MPS_3 *Appl. Phys.* A **74** S811–3

[22] Goossens D J 2010 Dipolar anisotropy in quasi-2D honeycomb antiferromagnet $MnPS_3$ *Eur. Phys. J.* B **78** 305–9

[23] Wildes A R, Zhitomirsky M E, Ziman T, Lançon D and Walker H C 2020 Evidence for biquadratic exchange in the quasi-two-dimensional antiferromagnet $FePS_3$ *J. Appl. Phys.* **127** 223903

[24] Chittari B L, Park Y, Lee D, Han M, MacDonald A H, Hwang E, Jung J and Jung J 2016 Electronic and magnetic properties of single-layer MPX_3 metal phosphorous trichalcogenides *Phys. Rev.* B **94** 184428

[25] Egami T and Billinge S J L 2003 *Underneath the Bragg Peaks: Structural Analysis of Complex Materials* (Oxford: Pergamon)
[26] Petkov V 2003 *Characterization of Materials* (New York: Wiley)
[27] Petkov V, Chapagain K, Shastri S and Ren Y 2020 Genesis in the charge density wave in the charge density wave state of 2H–$TaSe_2$ *Phys. Rev.* B **101** 121114(R)
[28] Petkov V and Ren Y 2021 Local structure memory effects in the polar and nonpolar phases of $MoTe_2$ *Phys. Rev.* B **103** 094101
[29] 2Dsemiconductorts (https://2dsemiconductors.com/feps3/)
[30] Guguchia Z *et al* 2017 Signatures of the topological s^{+-} superconducting order parameter in the type-II Weyl semimetal T_d–$MoTe_2$ *Nat. Commun.* **8** 1082
[31] Wright N G, Nelmes R J, Belmonte S A and McMahon M I 1996 Observation and modelling of preferred orientation in two-dimensional powder patterns *J. Synchrotron Radiat.* **3** 112–9
[32] Shannon R D 1976 Revised effective ionic radii and systematic studies of interatomic distances in halides and chalcogenides *Acta Crystallogr.* A **32** 751–67
[33] Muruyama C, Okabe M, Urushihara D, Asaka T, Fukuda K, Isobe M, Yamamoto K and Matsushita Y 2016 Crystallographic features related to a van der Waals coupling in the layered chalcogenide $FePS_3$ *J. Appl. Phys.* **120** 142114
[34] Petkov V 1989 RAD a program for analysis of XRD data from amorphous materials for personal computers *J. Appl. Crystallogr.* **22** 387–9
[35] Supplemental material.
[36] Gamble F R 1974 Ionicity, atomic radii, and structure in the layered dichalcogenides of group IVb, Vb, and VIb transition metals *J. Solid State Chem.* **9** 358–67
[37] Ouvgard G, Brec R and Rousel J 1985 Structural determination of some MPS_3 layered phases (M = Mn, Fe, Co, Ni and Cd) *Mater. Res. Bull.* **20** 1181–9
[38] Neal S N *et al* 2020 Symmetry and crossover in layered MPS_3 complexes (M = Mn, Fe, Ni) via near-field infrared spectroscopy *Phys. Rev.* B **102** 085408
[39] Goossens D J, James D, Dong J, Whitfield R E, Norén L and Withers R L 2011 Local order in layered $NiPS_3$ and $Ni_{0.7}Mg_{0.3}PS_3$ *J. Phys.: Condens. Matter.* **23** 065401
[40] Pauling L 1929 The principles determining the structure of complex ionic crystals *J. Am. Chem. Soc.* **51** 1010–26
[41] Le Flem G, Brec R, Ouvard G, Louisy A and Segransan P 1982 Magnetic interactions in the layer compounds MPX_3 (M = Mn, Fe, Ni; X = S, Se) *J. Phys. Chem. Solids* **43** 455–61
[42] Goodenough J B and Loeb A L 1995 Theory of ionic ordering, crystal distortion, and magnetic exchange due to covalent forces in spinels *Phys. Rev.* **98** 391–408
[43] Goodenough J B 1955 Theory of the role of covalence in the perovskite-type manganites [La, M(II)]MnO_3 *Phys. Rev.* **100** 564–73
[44] Kanamori J 1959 Superexchange interaction and symmetry properties of electron orbitals *J. Phys. Chem. Solids* **10** 87–98
[45] Ren W-N, Jin K-J, Wang J-s., Ge C, Guo E-J, Ma C, Wang C and Xu X 2021 Tunable electronic structure and magnetic anisotropy in bilayer ferromagnetic semiconductor $Cr_2Ge_2Te_6$ *Sci. Rep.* **11** 2744
[46] Otero Fumega A, Phillips J and Pardo V 2020 Controlled two-dimensional ferromagnetism in 1T-$CrTe_2$: the role of charge density wave and strain *J. Phys. Chem* C **124** 21047–53
[47] Kang S *et al* 2020 Coherent many-body exciton in van der Waals antiferromagnet $NiPS_3$ *Nature* **583** 785–9